Journal of Geodesy (2003) 76: 510–522
DOI 10.1007/s00190-002-0284-3

Journal of Geodesy

On geoid determination from airborne gravity

P. Novák[1], M. Kern[1], K.-P. Schwarz[1], M. G. Sideris[1], B. Heck[2], S. Ferguson[3], Y. Hammada[3], M. Wei[4]

[1] Department of Geomatics Engineering, The University of Calgary, 2500 University Drive NW, Calgary, Canada T2N 1N4
[2] Geodetic Institute, University of Karlsruhe, Englerstrasse 7, 76128 Karlsruhe, Germany
[3] Sander Geophysics Ltd, 260 Hunt Club Road, Ottawa, Canada K1V 1C1
[4] Intermap Technologies Ltd, 736 8 Avenue SW, Calgary, Canada T2P 1H4

Received: 10 August 2001 / Accepted: 12 April 2002

Abstract. Recent advances in the performance of scalar airborne gravimetry, routinely yielding gravity data with an accuracy as high as 1 mGal with a minimum spatial resolution (full wavelength) of 10 km, allow for the use of airborne gravity in precise geoid computations. Theoretical issues related to geoid determination from discrete samples of band-limited airborne gravity and practical geoid computations based on high-frequency synthetic data and actual observations are discussed. The mathematical model for geoid determination from band-limited airborne gravity which is introduced is based on Helmert's reduction of gravity/co-geoid and the application of the discretized integral formula developed specifically for airborne gravity data. Computational formulae are derived for the following specifications of airborne gravity data: almost-white observation noise, a band-limited frequency content of processed observations, and a smooth regular surface on which gravity observations are collected.

Two major applications of airborne gravity data for geoid determination are discussed. Airborne gravimetry can be used over areas with a sparse or no ground gravity coverage to provide the medium- to high-frequency components of the Earth's gravity field. These data can be used in combination with global gravity models for the computation of the gravimetric geoid. Airborne gravimetry can also be used to fill in gaps in existing ground gravity coverage (mainly in inaccessible areas). Both approaches are tested with actual airborne data observed using an inertially referenced airborne gravimeter at the Alexandria test range near Ottawa, Canada. Observed airborne gravity disturbances, combined with either ground or global gravity data, are used for the determination of the gravimetric geoid in the two applications outlined above. The combined solutions are compared to the latest official Canadian gravimetric geoid and to available GPS/levelling data in the area. Numerical results show that airborne data can be used for geoid determination with centimetre-level accuracy (medium- and high-frequency information) over areas with negligible topographical effects on gravity and the geoid.

Keywords: Geoid determination – Airborne gravimetry – Downward continuation

Correspondence to: P. Novák
Research Institute of Geodesy,
Topography and Cartography, Zdiby 98, 250 66 Czech Republic
Tel: +420 323 649 235, Fax: +420 323 649 236
e-mail: pnovak@pecny.asu.cas.cz

1 Introduction

Vertical separations of the geoid from a reference ellipsoid measured along the ellipsoidal normal can be estimated with sufficient accuracy by the Bruns theorem. The problem of geoid determination from airborne gravity can thus be formulated as follows: find the transformation of discrete observations of airborne gravity at flight level into the disturbing gravity potential at the geoid. Research on geoid determination from airborne gravity has been pursued for some time and results have appeared in the geodetic literature (see e.g. Forsberg et al. 1996; Kearsley et al. 1998). Generally, the research in this area started after airborne gravimetry proved to provide reasonably accurate information on the gravity field.

This contribution describes a new approach for geoid determination from airborne gravity that is rigorous, accurate, stable and complete. Before its mathematical model is formulated, airborne data are compared to ground gravity observations. Such a comparison helps in the understanding of the airborne model, especially of its differences from the generally well-known Stokes's solution commonly used for geoid determination from ground gravity observations. In the case of ground gravity observations, orthometric heights are usually

assumed to be known. These orthometric heights, estimated by spirit levelling and/or trigonometric height differences, are of varying accuracy depending on location, method and time of their determination (uncertainties at the level of tens of metres can be found in gravity databases). The knowledge of the orthometric heights leads to the derivation of gravity anomalies. As a consequence, the third boundary-value problem of potential theory must be used. In contrast, airborne gravimetry provides gravity data accompanied by accurate geodetic heights [derived from global positioning system (GPS) observables] that result in gravity disturbances and the second boundary-value problem of potential theory.

Ground and airborne gravity data also differ significantly in the geometric complexity of the corresponding observation surfaces. The ground data represent discrete samples of the continuous gravity field that are collected at a very complex topographical surface. Although this surface is usually considered (under some mild idealization) to be a Lipschitz boundary (Holota 2000), any boundary-value problem with such a boundary has an extremely difficult solution. To avoid such a solution, the problem is usually transformed into a free boundary-value problem with the unknown geoid as a corresponding boundary surface. In airborne gravimetry, the observation surface is represented by known smooth flight trajectories which can easily be approximated by a surface of a geocentric ellipsoid of revolution or a geocentric sphere. A fixed boundary-value problem can then be formulated and solved.

Another difference between ground and airborne gravity data lies in their observation errors. Although ground observations are generally more accurate, their quality is further deteriorated by the corresponding height information. Since the ground data are also collected over a long period of time, they usually face problems with their consistency, including all instrumentation effects. In contrast, airborne gravimetry provides data which result in consistent samples of gravity covering certain geographically limited areas. Recent investigations have shown that observation noise has almost a constant power over the frequency spectrum currently considered in airborne gravimetry (Bruton 2000). The observation noise of airborne gravity is thus similar to white noise.

The most significant difference between ground and airborne gravity observations is, however, in their frequency content. In contrast to ground observations, airborne data must be processed prior to their use for geoid determination. In order to remove the high-frequency observation noise caused mainly by the flight dynamics and GPS data, the recorded signal is low-pass filtered, which results in the removal of all high frequencies from airborne gravity. This is a major drawback of airborne gravimetry which allows, however, for the formulation of a new mathematical model that avoids any numerically unstable solutions to inverse integral formulae. The specifications of airborne gravity data compared to ground observations are listed in Table 1, which summarizes the main differences of these two data sets and their consequences for geoid determination.

Table 1. Properties of ground versus airborne gravity data

Specification	Ground data	Airborne data
Observed heights	orthometric	geodetic
Observation surface	high level of complexity	smooth
Boundary values	gravity anomalies	gravity disturbances
Boundary-value problem	first/third	second
Boundary surface	topography/geoid	flight level
Observation noise	varying (often unknown)	approximately white
Frequency content	full spectrum	band-limited spectrum

This manuscript is organized as follows: Theoretical formulations of the mathematical model are given in Sect. 2. A high-frequency synthetic geopotential model is then used in Sect. 3 to verify the correctness of the presented formulae and software, and for evaluation of the noise propagation through the mathematical model. The same data configuration, i.e. flight elevation and geographical extent, is used as in the case of actually observed airborne data. Airborne data, collected in the Alexandria test range near Ottawa, Canada, using an inertially-referenced airborne gravimeter, are processed in Sect. 4. The quality of the band-limited geoid models, based on a combination of airborne/global data and airborne/ground data, is assessed using the reference geoid computed from ground data only. Obtained results are discussed in Sect. 5, which also includes the conclusions of the presented research.

2 Mathematical model

In airborne gravimetry, gravity observations are accompanied by precise GPS-based positioning (precise in terms of the latest developments of kinematic GPS positioning) which results in geodetic coordinates (h, ϕ, λ) of each observation point. In the following, the spherical harmonic functions and the spherical approximation of the geoid are used. The transformation of the geodetic coordinates (Jacobi's ellipsoidal coordinates) into the geocentric spherical coordinates can easily be done for a selected reference sphere (Heiskanen and Moritz 1967). Correspondingly, the triad $(r, \varphi, \lambda) = (r, \Omega)$ defines the position of the point of interest in the geocentric spherical coordinate system and the reference geocentric sphere is defined in terms of radius R. It is assumed that flight trajectories can be approximated by a geocentric sphere of constant radius $r = R + D$ with D being the vertical separation of flight level above the reference sphere. The topography can be described by a two-dimensional (2-D) function $r(\Omega) = r_g(\Omega) + H(\Omega) \approx R + H(\Omega)$; $r_g(\Omega)$ is the

geocentric radius of the geoid and $H(\Omega)$ is the orthometric height. Figure 1 shows the geometry of the problem. Knowledge of the precise geodetic height h at each observation point allows derivation of gravity disturbances

$$\delta g(R+D,\Omega) = g(R+D,\Omega) - \gamma(R+D,\Omega) \quad (1)$$

where g stands for the magnitude of observed airborne gravity and γ for the magnitude of normal gravity computed by a Somigliana–Pizzetti formula for a selected international reference ellipsoid. Due to high-frequency observation noise in the gravity signal, airborne gravity disturbances must be processed by a low-pass filter. This operation results in the low-frequency gravity disturbances δg^{ℓ}

$$\delta g^{\ell}(R+D,\Omega) = \mathcal{F}^{\ell}[\delta g(R+D,\Omega)] \quad (2)$$

In the following, ℓ is the maximum degree (cut-off frequency of the filter) which can be resolved from airborne gravimetry (currently, a maximum spatial resolution of 10 km can be expected, corresponding to degree $\ell \approx 2000$ in terms of the spherical harmonic expansion). A typical low-pass filter $\mathcal{F}$, used in processing of airborne gravity data, is described in Bruton (2000). Reference gravity disturbances, generated from the global geopotential model (GGM) up to degree $k-1$, are then subtracted from the low-frequency gravity disturbances δg^{ℓ} obtained from Eq. (2). The maximum degree L (greater than or equal to $k-1$ for $k \ll l$) of currently available geopotential models is 360. Results are the band-limited gravity disturbances δg^{b} at flight level $R+D$

$$\delta g^{b}(R+D,\Omega) = \delta g^{\ell}(R+D,\Omega) - \frac{GM}{(R+D)^2} \times \sum_{n=2}^{k-1}(n+1)\left(\frac{R}{R+D}\right)^{n} T_n(\Omega) \quad (3)$$

GM stands for the geocentric gravitational constant, and Laplace's coefficients T_n of the disturbing gravity potential T can be derived from the available GGM up to $n = 360$. The resulting band-limited gravity disturbances δg^{b} can be written in the spectral form

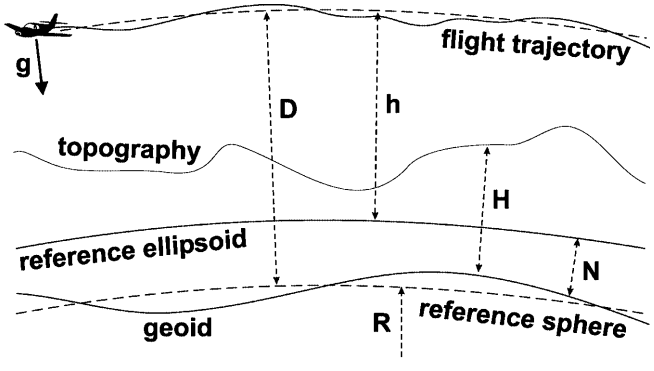

Fig. 1. Geometry of geoid determination from airborne gravity

$$\delta g^{b}(R+D,\Omega) = \frac{GM}{(R+D)^2}\sum_{n=k}^{\ell}(n+1)\left(\frac{R}{R+D}\right)^{n} T_n(\Omega) \quad (4)$$

with the band-limited spectrum between the frequency-equivalent degrees k and ℓ. Current maximum values are 361 for k (if the complete GGM is used) and approximately 2000 for ℓ.

The transformation of the band-limited gravity disturbances δg^{b} at flight level $R+D$ (vertical gradient of the band-limited disturbing gravity potential) into the band-limited disturbing gravity potential T^{b} at the geoid R can be performed using boundary-value problems of potential theory. This requires, however, that the Earth's gravity field is harmonic everywhere above the geoid, i.e. the band-limited disturbing gravity potential must be expandable into a convergent series of elementary harmonic functions, such as spherical harmonics. Band-limited airborne gravity disturbances in Eq. (3), which would correspond to such a harmonic field, can be derived by applying an appropriate gravity reduction. There are many possibilities for the derivation of the harmonic gravity field. Generally, the direct topographical effect must be applied

$$\delta g^{h,b}(R+D,\Omega) = \delta g^{b}(R+D,\Omega) + \delta A^{b}(R+D,\Omega) \quad (5)$$

where δA^{b} is the band-limited direct effect on airborne gravity. The direct effect accounts for the change of the Earth's gravity due to 'harmonization' of the external Earth's gravity field.

The evaluation of the band-limited direct effect on airborne gravity δA^{b} using the second Helmert condensation (see e.g. Heck 1993) is briefly discussed in this article. Considering mass-preserving condensation (the mass of the topography equals the mass of the condensed topography), the band-limited direct topographical effect on airborne gravity reads (Novák et al. 2001)

$$A^{b}(R+D,\Omega) = -2\pi\frac{G\varrho}{R}\sum_{n=k}^{\ell}\frac{n(n+1)}{2n+1}\left(\frac{R}{R+D}\right)^{n+2} H_n^2(\Omega) - 2\pi\frac{G\varrho}{R^2}\sum_{n=k}^{\ell}\frac{n(n+1)(n+3)}{2n+1} \times \left(\frac{R}{R+D}\right)^{n+2} H_n^3(\Omega) + \mathcal{O}\left[\frac{H_n^4(\Omega)}{R^3}\right] \quad (6)$$

with G the universal gravitational constant and ϱ the constant mean topographical mass density. $\mathcal{O}$ stands for the Landau symbol. The complex Laplace harmonics of the squared topographical heights are defined as follows:

$$H_n^2(\Omega) = \sum_{m=-n}^{n} H_{n,m}^2 Y_{n,m}(\Omega) = \frac{2n+1}{4\pi}\iint_{\Theta} H^2(\Omega')P_n(\cos\psi)\mathrm{d}\Omega' \quad (7)$$

and the complex Laplace harmonics of the cubed topographical heights as follows:

$$H_n^3(\Omega) = \sum_{m=-n}^{n} H_{n,m}^3 Y_{n,m}(\Omega) = \frac{2n+1}{4\pi} \iint_{\Theta} H^3(\Omega') P_n(\cos\psi) \mathrm{d}\Omega' \quad (8)$$

In Eqs. (7) and (8), Θ stands for the full spatial angle. The corresponding spherical harmonic functions $Y_{n,m}$ read (Hobson 1931)

$$Y_{n,m}(\Omega) = \mathrm{e}^{im\lambda} P_{n,m}(\sin\varphi), \quad \text{for } n \geq m \wedge i = \sqrt{-1} \quad (9)$$

with $P_{n,m}$ being the associated trigonometric Legendre functions of the first kind (Hobson 1931). The second method of Helmert reduction of gravity is usually applied due to the relatively small values of both the direct and indirect effects. The impact of the unknown density distribution ϱ and erroneous topographical heights H can be minimized in this way, especially over mountainous areas. On the other hand, the gravity field that is obtained by this method can be even rougher than the free-air gravity field, which complicates some numerical evaluations, such as the downward continuation. Generally, less restrictive specifications (such as the discretization step of topographical masses) are required for correct evaluation of the direct effect on airborne gravity than for evaluation of the corresponding effect on ground gravity. For more details on this, see Novák et al. (2001).

In the spherical approximation of the geoid by the geocentric reference sphere, the transformation of the reduced band-limited gravity disturbances $\delta g^{h,b}$ at flight level into the band-limited disturbing potential $T^{h,b}$ on the geoid, i.e. at $r_g \approx R$, can be written as follows:

$$\begin{aligned} &\nabla^2 T^{h,b}(r,\Omega) = 0 \quad \text{for } r > R \\ &\delta g^{h,b}(r,\Omega) = -\left.\frac{\partial T^{h,b}(r,\Omega)}{\partial r}\right|_r \quad \text{for } r = R + D \\ &T^{h,b}(r,\Omega) = \mathcal{O}(r^{-k-1}) \quad \text{for } r \to \infty \end{aligned} \quad (10)$$

The solution to the problem of Eqs. (10) exists and is unique, but can be unstable. The original improperly posed problem can be transformed to a properly posed problem due to the band-limited character of the airborne gravity data. Moreover, the airborne data are collected on a smooth surface which can easily be approximated by a sphere. Therefore, a direct solution of the pseudo-boundary-value problem of Eqs. (10) for the band-limited disturbing gravity potential $T^{h,b}$ can be derived (Novák and Heck 2002). It results in the following solution formula for the reduced band-limited gravity disturbances $\delta g^{h,b}$ given at flight level $R + D$:

$$T^{h,b}(R,\Omega) = \frac{R+D}{4\pi} \iint_{\Theta} \delta g^{h,b}(R+D,\Omega') \mathcal{J}^b(R,\psi,R+D) \mathrm{d}\Omega' \quad (11)$$

The band-limited integration kernel $\mathcal{J}^b$ reads (Novák and Heck 2002)

$$\mathcal{J}^b(R,\psi,R+D) = \sum_{n=k}^{\ell} \frac{2n+1}{n+1} \left(\frac{R+D}{R}\right)^{n+1} P_n(\cos\psi) \quad (12)$$

The Legendre polynomials P_n can easily be generated by a convenient recurrence relation of the form (Paul 1973)

$$P_n(\cos\psi) = \frac{2n-1}{n}\cos\psi P_{n-1}(\cos\psi) - \frac{n-1}{n} P_{n-2}(\cos\psi), \quad \text{for } n \geq 2 \quad (13)$$

with $P_0(\cos\psi) = 1$ and $P_1(\cos\psi) = \cos\psi$. Applying a simple quadrature rule, and considering the truncation error resulting from spherical cap integration (the full spatial angle Θ is replaced by the spherical cap of radius ψ_o), the discretized integral of Eq. (11) takes the form

$$\begin{aligned} T^{h,b}(R,\Omega_i) &- \frac{GM}{2(R+D)} \times \sum_{n=k}^{L} (n+1) \left(\frac{R}{R+D}\right)^{n+1} Q_n(D,\psi_o) T_n(\Omega_i) \\ &= \frac{R+D}{4\pi} \sum_{j=1}^{K} \delta g^{h,b}(R+D,\Omega_j) \times \mathcal{J}^b(R,\psi_{ij},R+D) \Delta\Omega_j, \quad \text{for } k < L \end{aligned} \quad (14)$$

where $\Delta\Omega_j$ is the area of the trapezoidal cell corresponding to the jth data point, K stands for the number of points within the spherical cap of radius ψ_o, and L is the maximum degree of the GGM. If the full reference field is removed from gravity data, the truncation errors cannot be computed. The truncation coefficients Q_n related to the function $\mathcal{J}^b$ are

$$Q_n(D,\psi_o) = \sum_{m=k}^{\ell} \frac{2m+1}{m+1} \left(\frac{R+D}{R}\right)^{m+1} R_{n,m}(\psi_o) \quad (15)$$

The coefficients $R_{n,m}$

$$R_{n,m}(\psi_o) = \int_{\psi_o}^{\pi} P_n(\cos\psi) P_m(\cos\psi) \sin\psi \ \mathrm{d}\psi \quad (16)$$

can conveniently be computed by an iterative expression [Paul 1973; Eq. (5)]. The matrix form of Eq. (14) can be concisely written as

$$\mathbf{T}^{\mathbf{h},\mathbf{b}}(\mathbf{R}) = \mathbf{A}\delta\mathbf{g}^{\mathbf{h},\mathbf{b}}(\mathbf{R}+\mathbf{D}) \quad (17)$$

where the unknown vector $\mathbf{T}^{\mathbf{h},\mathbf{b}}(\mathbf{R})$ is reduced by the contribution of the corresponding remote-zone data given by the spherical harmonic series on the left-hand side of Eq. (14). Since no inverse is involved in Eq. (17), there are no instabilities in the numerical evaluation of this relationship. The off-diagonal entries of the matrix operator $\mathbf{A}$ within the integration cap of radius ψ_o can be defined as

$$A_{ij} = \frac{R+D}{4\pi}\mathcal{J}^b(R,\psi_{ij},R+D)\Delta\Omega_j, \quad \psi_{ij} < \psi_o \tag{18}$$

The corresponding diagonal entries are then given as

$$A_{ii} = \frac{R+D}{2}\sum_{n=k}^{\ell}\frac{2n+1}{n+1}\left(\frac{R+D}{R}\right)^{n+1}R_n(\psi_o) - \frac{R+D}{4\pi}\sum_{j=1,j\neq i}^{k}\mathcal{J}^b(R,\psi_{ij},R+D)\Delta\Omega_j \tag{19}$$

where k stands for the number of points within the spherical cap. The coefficients R_n read

$$R_n(\psi_o) = \int_{\psi_o}^{\pi} P_n(\cos\psi)\sin\psi \; \mathrm{d}\psi \tag{20}$$

which can conveniently be computed by the same iterative expression as the coefficients $R_{n,m}$; see Eq. (16) for $m = 0$. The radius ψ_o of the spherical cap in the integral formula of Eq. (14) should correspond to the required bandwidth of the geoid (the larger the cap, the longer the wavelengths of the geoid which can be determined) computed from the local gravity data. A value of $\psi_o \leq 6^\circ$ is usually used due to fast attenuation of the integration function $\mathcal{J}^b$.

The band-limited geoid is obtained by Bruns's formula (Heiskanen and Moritz 1967)

$$N^b(\Omega) = \frac{T^{h,b}(R,\Omega)}{\gamma(\varphi)} + \frac{\delta V^b(R,\Omega)}{\gamma(\varphi)} \tag{21}$$

where γ is the magnitude of normal gravity at the ellipsoid computed for latitude φ. The second term on the right-hand side of Eq. (21) is the indirect topographical effect on the geoid. Considering again mass-preserving condensation, the band-limited residual topographical potential δV^b at the geoid can be computed as follows (Novák et al. 2001):

$$\delta V^b(R,\Omega) = -2\pi G\varrho\sum_{n=k}^{\ell}\frac{n+1}{2n+1}H_n^2(\Omega) + 2\pi\frac{G\varrho}{3R}\sum_{n=k}^{\ell}\frac{(n+1)(n-2)}{2n+1}H_n^3(\Omega) + \mathcal{O}\left[\frac{H_n^4(\Omega)}{R^2}\right] \tag{22}$$

Finally, the low-frequency geoid is obtained by restoring the reference gravity field computed by the spherical harmonic expansion from the GGM

$$N^\ell(\Omega) = N^b(\Omega) + R\sum_{n=2}^{k-1}T_n(\Omega) \tag{23}$$

where an approximation $GM/R^2 \doteq \gamma$ is used. In the solution N^ℓ, all frequencies above the cut-off value ℓ are obviously missing. The contribution of this part of the spectrum, for $\ell \approx 2000$, is rather small and currently within the observation noise propagated through the model.

The entire scheme for the derivation of the band-limited gravimetric geoid from airborne gravity outlined in this section is shown Fig. 2. The entire approach is based on the assumptions that the reduced gravity field as close to the actual harmonic field above the geoid as possible can be derived and that the possible misfit of these two fields would not significantly affect practical geoid computations. The solution is derived in terms of the Green integral formula with the integration kernel reflecting the shape of the boundary surface, i.e. the geocentric sphere of radius $R + D$. The values of the sub-integral function also refer to flight level $R + D$. Another problem arises from the fact that the Green integral formula should be evaluated over the full spatial angle Θ, which requires global knowledge of the gravity data. Although truncation errors can be computed, small errors can still be expected due to imperfections (especially in high frequencies) of currently available GGMs.

3 Numerical tests using synthetic gravity data

The high-frequency synthetic geopotential model (SGM) was used to verify numerically the mathematical model described in Sect. 2 and to test the numerical accuracy of developed programs; for details see Novák et al. (2001). Its spherical harmonic coefficients of degrees and orders 361 to 2160 were created as a smooth extension of EGM96 (Lemoine et al. 1998) with a comparable magnitude to the GPM98b (Wenzel 1998). This synthetic model was used for the computation of the band-limited gravity disturbances δg^b at flight level $R + D$ and the band-limited geoid N^b for degrees 181–2160, which correspond to spatial resolutions of approximately 10–100 km full wavelength. The same data configuration and the same mean flight height D as for the actual airborne gravity data observed at the Alexandria test range (processed in the next section) were utilized in this test, see Fig. 3. This corresponded approximately to 3000 discrete values of the band-limited gravity disturbances referred to the average flight height of

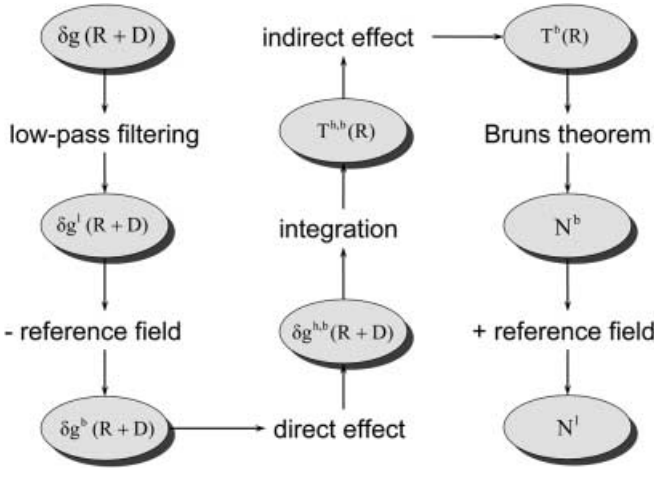

Fig. 2. Computation scheme of geoid determination from airborne gravity

$D = 604$ m. A random noise of 1.5 mGal was introduced into these gravity disturbances. Its characteristic values can be found in the first row of Table 2.

Synthetic degree 181–2160 airborne gravity disturbances δg^b, generated along actual flight lines (see Fig. 3), were used for prediction of data on a regular geographical grid with a homogeneous spatial resolution of 300 arcsec. This spatial resolution corresponds to the horizontal spacing between individual flight lines of approximately 10 km. Least-squares collocation (LSC) was used for the prediction of gravity data on the regular grid (Moritz 1980). The data area was expanded for additional gravity disturbances that were computed only from EGM96, i.e. for $k = 181$ and $\ell = L = 360$. These data were utilized to minimize edge effects in the discretized integral formula [Eq. (14)] deployed in the computations. The grid of the synthetic degree 181–2160 airborne gravity disturbances was used to compute values of the degree 181–2160 disturbing gravity potential T^b at level R by the discretized integral formula in Eq. (14). The degree 181–2160 geoid N^b was finally determined using the spherical Bruns formula. This solution was tested against values generated directly by the spherical harmonic expansion. The computational scheme of the entire test is shown in Fig. 4. The statistics of the obtained differences are compiled in Table 2; row 2 contains statistics of the gravity errors after the least-squares (LS) prediction, and the geoid errors ε^N after the numerical integration are given in row 3. The geoid errors ε^N are also plotted in Fig. 5. These differences, which theoretically should be equal to zero everywhere, can be used for accuracy evaluation of the mathematical model represented by the combined use of LSC and the discretized integral formula in Eq. (14), i.e. model and numerical errors.

Another test was performed in order to simulate computations used for actually observed ground and airborne gravity data deployed in the next section. Its main purpose was to compare the accuracy of the mathematical models and their computer realization used for processing of airborne gravity data as described in this manuscript, and for the processing of ground gravity data based on the inverse solution to the discretized Abel–Poisson and Stokes integrals. Input data for the airborne model were represented by synthetic degree 181–2160 gravity disturbances and for the ground model by synthetic degree 181–2160 gravity anomalies. The tests were performed for both noise-free data and erroneous data, which were obtained by adding 1.5-mGal random noise to both ground and airborne data sets. It should be noted that this noise represents quite well the noise in actual airborne data, but its applicability for ground data could easily be challenged. The results of this test are shown in Table 3. Values in this table represent the statistics of the differences obtained after relating the results from the ground and airborne models to the reference solution, which is represented by the degree 181–2160 geoid computed directly from the SGM by the series expansion. The results for the ground and airborne models were then also compared with respect to each other.

The values in Table 3 can be used to draw the following conclusions. For the noise-free data, the expected accuracy of both models was approximately at the level of 2–3 cm with a comparable bias of 2 cm. Both the ground and airborne noise-free data yielded almost identical geoidal heights; the standard deviation of the fit was equal to 0.7 cm. The situation for the erroneous data did not change significantly. The fit of both solu-

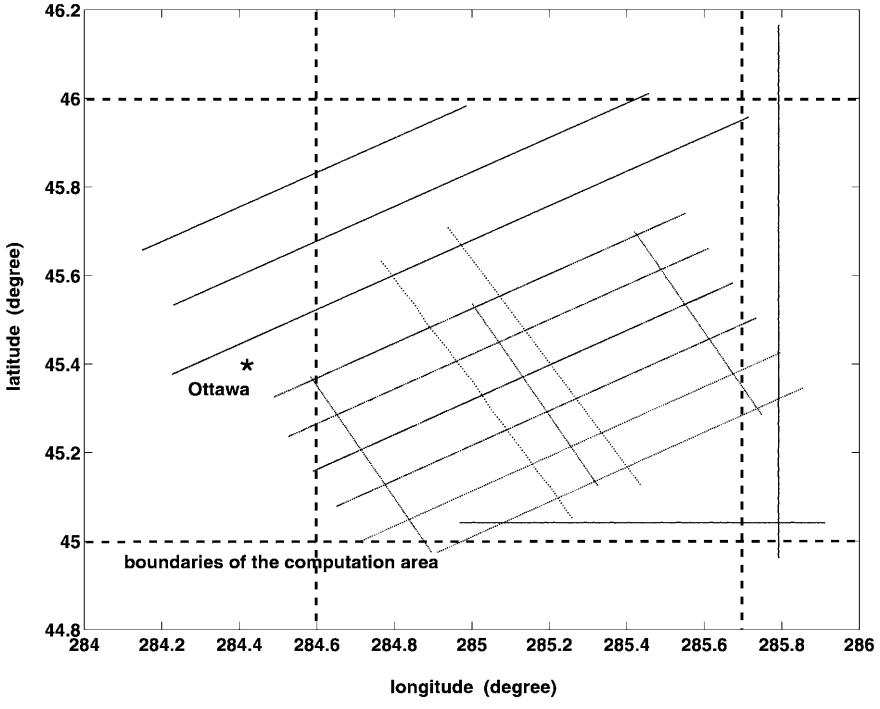

Fig. 3. Alexandria test range and flight-line configuration

Table 2. Random noise in synthetic gravity and its propagation through the model

Noise	Minimum	Maximum	Mean	Sigma	Unit
Initial (white)	−4.163	4.608	0.070	1.420	mGal
After prediction	−5.235	5.376	−0.042	1.410	mGal
After integration	−0.049	0.047	−0.012	0.021	m

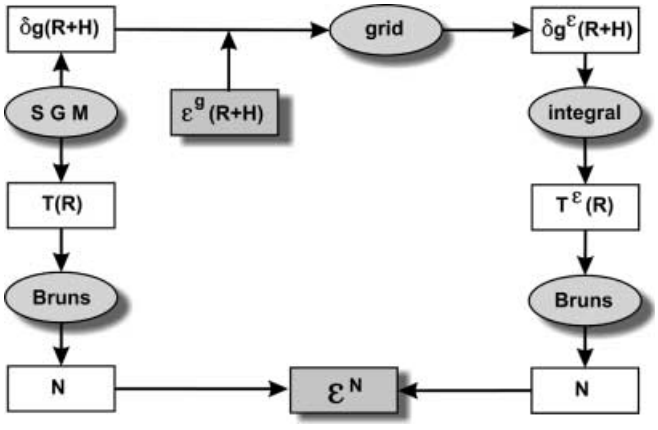

Fig. 4. Scheme of the test procedure using the synthetic data

tions with respect to the reference geoid was still at the level of 2–3 cm with the same bias of 2 cm. The fit of the geoid based on the ground and airborne models was in this case two times worse than that for the noise-free data but it still remained at a reasonable 1.5 cm. We can conclude that the numerical accuracy obtained using the ground and airborne model was at the centimetre level for both the errorless and noisy data, assuming the resolution, elevation and noise level of gravity data used in these tests. Both models provided almost identical solutions of the geoid, assuming again the data characteristics used in the tests.

The tests described above provided information on the expected accuracy of the band-limited geoid computed by the approach adopted in the computation scheme. These tests could not, however, give any information on the expected accuracy of additional computational steps, especially of those related to the gravity/co-geoid reduction. A complete synthetic gravity field, currently under construction (IAG Special Study Group 3.177), would have to be used in this case to evaluate the accuracy of complete geoid determination. Due to the small values of topographical effects in the test area, these steps did not affect the solutions significantly.

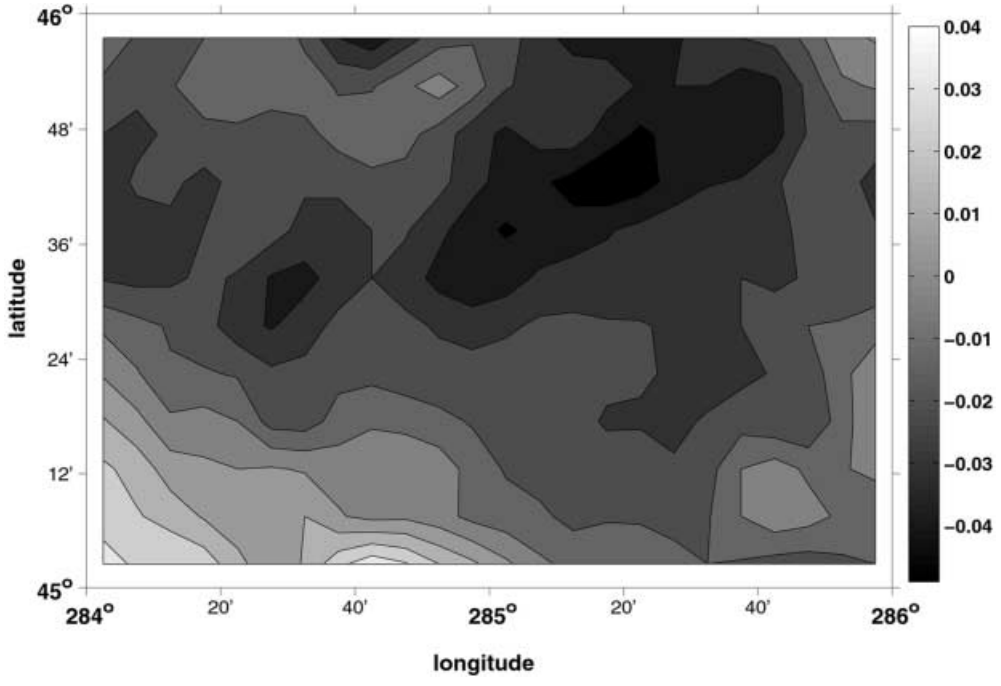

Fig. 5. Propagation of random errors through the model (m)

Table 3. Accuracy of geoid models based on airborne and ground synthetic data (m)

Solution	Noise	Minimum	Maximum	Mean	Sigma	RMS
Airborne–reference	no	−0.069	0.058	0.022	0.025	0.033
	yes	−0.068	0.069	0.020	0.029	0.035
Ground–reference	no	−0.045	0.053	0.021	0.022	0.031
	yes	−0.056	0.064	0.022	0.024	0.032
Airborne–ground	no	−0.016	0.024	0.000	0.007	0.007
	yes	−0.043	0.044	0.002	0.015	0.015

4 Numerical evaluations using actual airborne data

The entire computational scheme as described in Sect. 2 was applied in processing of actual airborne data observed by the Canadian geophysical company Sander Geophysics Ltd. at the Alexandria test range. Figure 3 shows the geometry of flight lines used for collection of gravity data using the inertially referenced (Schuler-tuned system) airborne gravimeter AIRGrav during an observation campaign in April 2000. Additional data were then observed in May 2001. The test observations, reported in Argyle et al. (2000), indicate the relatively high accuracy of the gravimeter. Data repeatability of better than 1 mGal for spatial resolutions up to 5 km can be obtained. Good temperature control of gravity sensors and modelling is responsible for long-period stability of 1 mGal or better.

The Alexandria test range, known for significant changes of gravity induced by density variations rather than rough topography, is very suitable for testing the accuracy of geoid determination from airborne gravity. The advantage of this test range consists of small (almost negligible) topographical effects on gravity (direct effect) and the co-geoid (indirect effect). Thus these effects had only a little impact on the main objective of the test: use of the actual airborne gravity observations for geoid determination. The topography of the test range and its surrounding area, based on the 30×30 arcsec digital elevation model, is shown in Fig. 6, which clearly shows the flat character of the topography in this region. The gravity field in terms of the ground gravity anomalies is shown in Fig. 7. Statistics of these two parameters are given in Table 4.

The band-limited disturbing gravity field, derived from observed airborne gravity, was predicted first on the homogeneous 300×300 arcsec geographical grid. Band-limited airborne gravity disturbances δg^b were next reduced using the Helmert reduction procedure and the spherical harmonic model GTM3A of maximum degree 1800 (Wenzel 1999). Values of the direct topographical effect on gravity at flight level are shown in Fig. 8. The magnitude of the direct topographical effect remained within the noise level of the airborne gravity data (1.5 mGal) and its effect on the final geoid was thus very small in this case. Values of the indirect topographical effect on the co-geoid are plotted in Fig. 9. Elementary statistics of these two effects can also be found in Table 4. As pointed out already, the small magnitude of both topographical effects is a significant advantage of the Alexandria test range. Over areas with more complex topography, the topographical effects play a significant role in geoid determination. In extreme cases, such as the Rocky Mountains, the topographical effects can easily reach values that are comparable to the magnitude of the disturbing gravity. The topographical effects must then be evaluated very carefully using the best-available height and density data. Despite recent significant advances in the modelling of the topographical effects, these values remain one of the limiting factors for resolving the geoid with centimetre accuracy. Due to the almost constant height associated with airborne gravity data, the atmospheric reduction of gravity can easily be achieved by adding the constant direct atmospheric effect of 0.81 mGal to all values of airborne gravity. The indirect atmospheric effect on the geoid is negligibly small (6 mm) for the accuracy level of the current airborne data.

Due to the limited geographical extent of the computation area (approximately $1^\circ \times 1^\circ$), only the solution of band-limited gravimetric geoids could be attempted. In terms of the spherical harmonic expansion, the term 'band limited' stands for degrees $181 \leq n \leq 2000$. Any longer wavelengths, i.e. lower frequencies, could not be determined from this area, and shorter wavelengths, i.e.

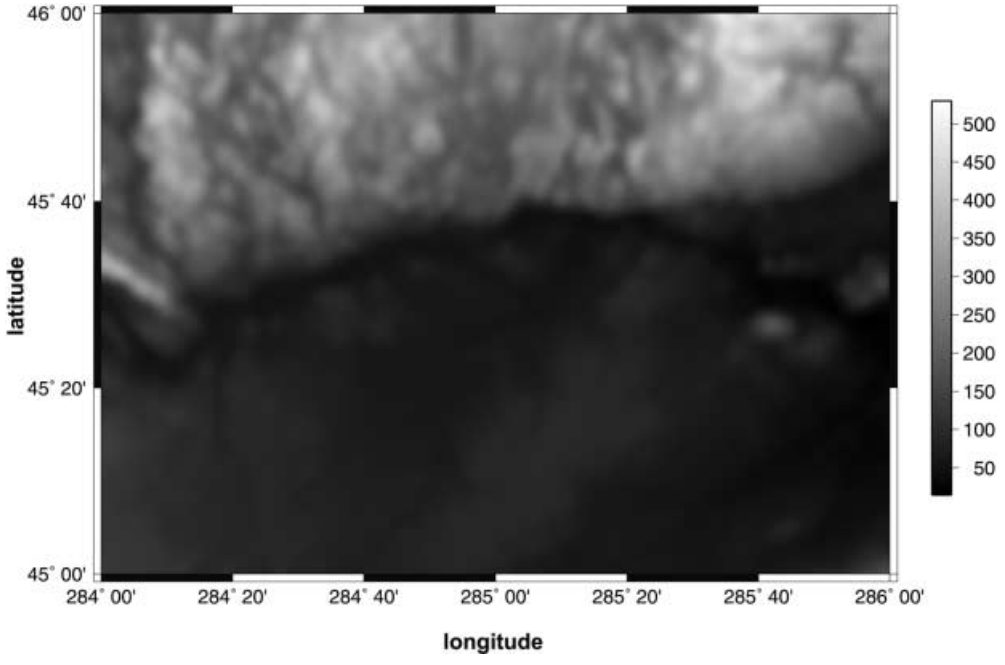

Fig. 6. Topography of the Alexandria test range (m)

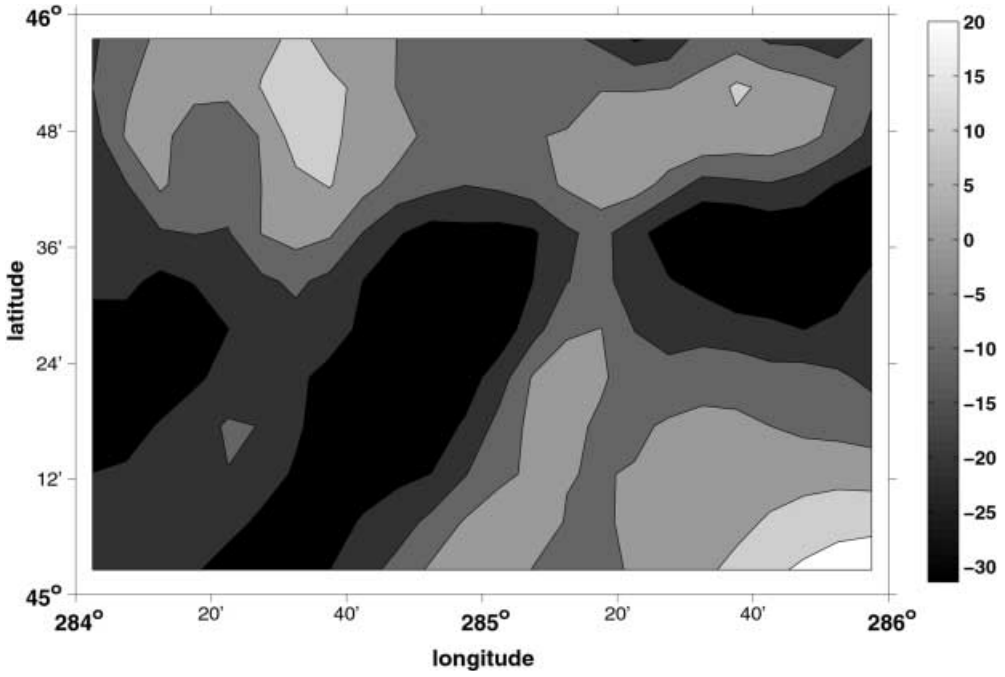

Fig. 7. Anomalous gravity field of the Alexandria test range (mGal)

higher frequencies, were missing due to the filtering of the airborne data and the averaging of ground data. The first geoid model was derived combining only the band-limited airborne and global gravity data. This combined band-limited disturbing gravity field at flight level $D = 604$ metres is shown in Fig. 10. Airborne gravity data are clearly distinguishable from global gravity, mainly due to their different frequency contents: airborne data contain spherical harmonic degrees of approximately $181 \leq n \leq 2000$ while the global gravity data contain only $181 \leq n \leq 360$. The second geoid model was then derived combining the band-limited ground and airborne gravity data. These data sets, combined at the geoid, are shown in Fig. 11. Airborne data can hardly be distinguished in this figure, indicating the reasonable consistency of these two gravity data sets. The frequency content of ground and airborne data was in this case approximately the same, i.e. $181 \leq n \leq 2000$, since the ground data represented mean values computed by averaging point gravity observations within 300×300 arcsec geographical cells. In both cases, the data combination was achieved by simple merging of the two data sets.

In order to evaluate the accuracy of both geoid models, a reference geoid was computed using only the ground gravity anomalies obtained from the Canadian gravimetric database; see Fig. 12. A classical approach, based on the convolution of the inverse solution to the discretized Abel–Poisson integral with the Stokes function at the reference sphere, was deployed. Due to a favourable ratio of the data spacing to their elevation, no numerical instabilities were observed during the downward-continuation procedure. An iterative approach was used for evaluation of the inverse solution. Ground gravity anomalies were reduced prior the numerical integrations for the direct effects, and the obtained co-geoid was corrected for the corresponding indirect effects. Since this approach is generally well known, no details are given here of the solution. This reference solution was added to the global geoid computed from EGM96 and compared to the latest official Canadian geoid model GSD95 (Véronneau 1995). The agreement of these two geoids was about 1.2 cm (standard deviation of the fit) after removing a constant bias. The Geodetic Survey Division (GSD) model has a very good agreement to GPS/levelling data in the area and a centimetre-level fit can generally be expected. It was thus concluded that the derived reference solution represents the medium and short wavelength of the geoid with centimetre-level accuracy. Therefore it can successfully be used as a reference for the corresponding wavelengths of the geoid computed from airborne data.

The first geoid model, based on combination of airborne and global gravity data, was subsequently derived using the approach outlined in Sect. 2. The band-limited gravity disturbances at flight level were first reduced by the corresponding direct topographical effect, see Eq. (5). The reduced band-limited gravity disturbances $\delta^{h,b}$ were transformed from flight level $R + D$ via the discretized integral formula in Eq. (14) into band-limited disturbing gravity potential $T^{h,b}$ at the geoid, approximated by the sphere of radius R. The band-limited co-geoid $N^{h,b}$ was then computed using the Bruns

Table 4. Statistics of topographical heights, gravity anomalies and topographical effects in Alexandria test range

Parameter	Minimum	Maximum	Mean	Sigma	Unit
Topographical height	24.8	461.3	137.4	95.8	m
Ground gravity anomaly	−31.45	26.28	−8.56	12.51	mGal
Direct effect	−0.552	0.773	0.074	0.144	mGal
Indirect effect	−0.022	0.000	−0.003	0.004	m

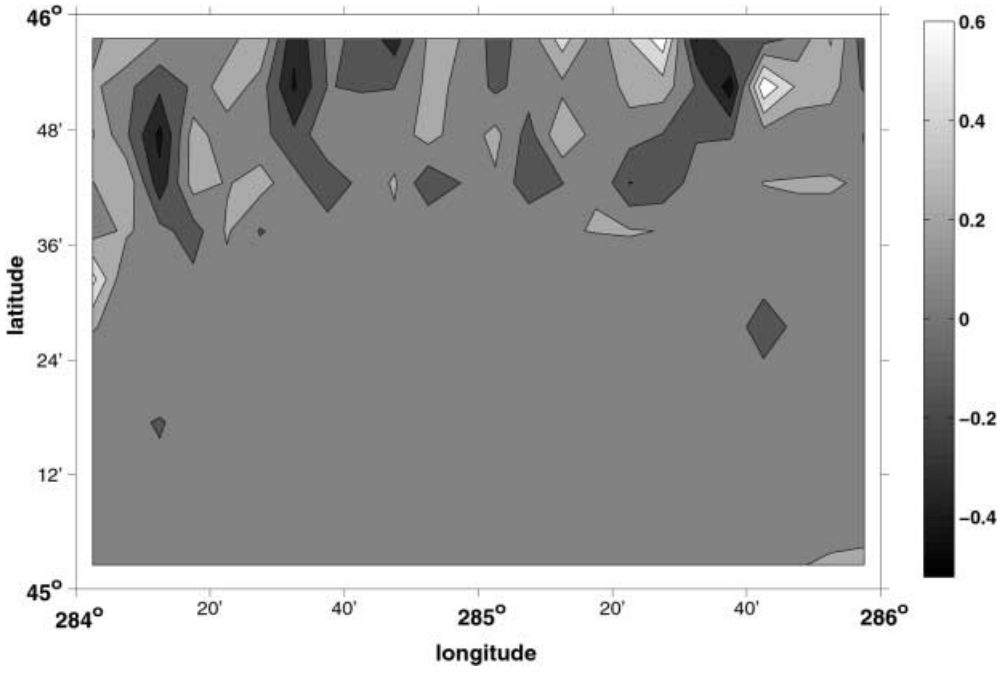

Fig. 8. Direct topographical effect on airborne gravity (mGal)

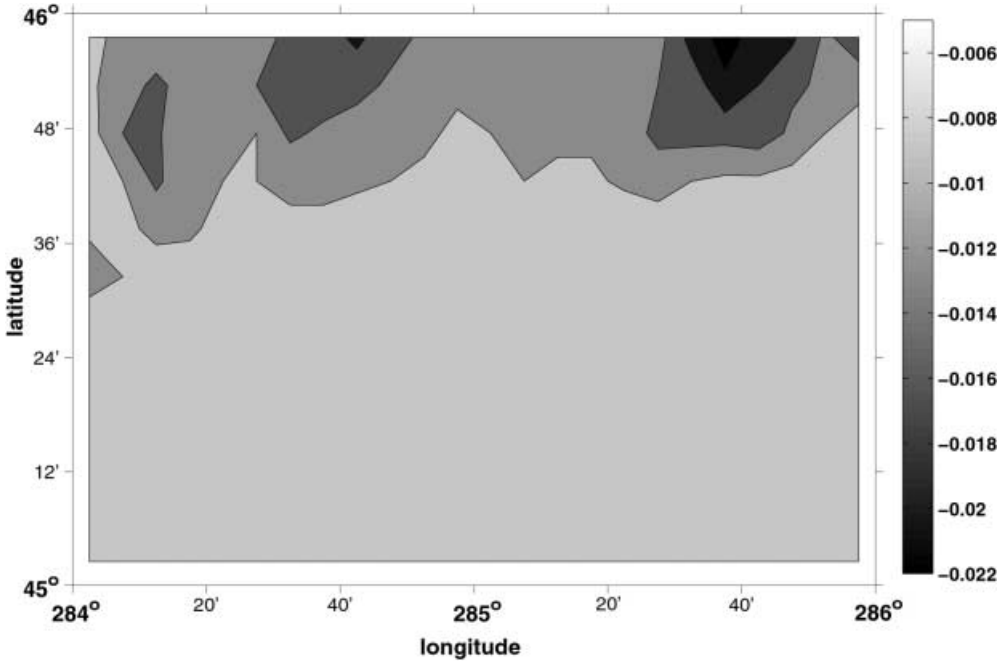

Fig. 9. Indirect topographical effect on the co-geoid (m)

formula and corrected for the corresponding indirect topographical effect in Eq. (21). The second geoid model, based on a combination of airborne and ground data, was derived using a slightly modified approach. The band-limited airborne gravity disturbances were first downward continued from flight level to the reference sphere using a stable solution described in Novák and Heck (2002)

$$\delta g^{h,b}(R,\Omega) = \frac{1}{4\pi}\int\int_{\Theta} \delta g^{h,b}(R+D,\Omega') \times \mathcal{K}^{b}(R,\psi,R+D)\mathrm{d}\Omega' \tag{24}$$

with the band-limited integration kernel

$$\mathcal{K}^{b}(R,\psi,R+D) = \sum_{n=k}^{\ell}(2n+1)\left(\frac{R+D}{R}\right)^{n+2} P_n(\cos\psi) \tag{25}$$

The ground band-limited gravity anomalies were also downward continued to the reference sphere using the inverse solution to the discretized Abel–Poisson integral equation. Airborne gravity disturbances were transformed into anomalies and combined with the ground gravity anomalies. The band-limited co-geoid was

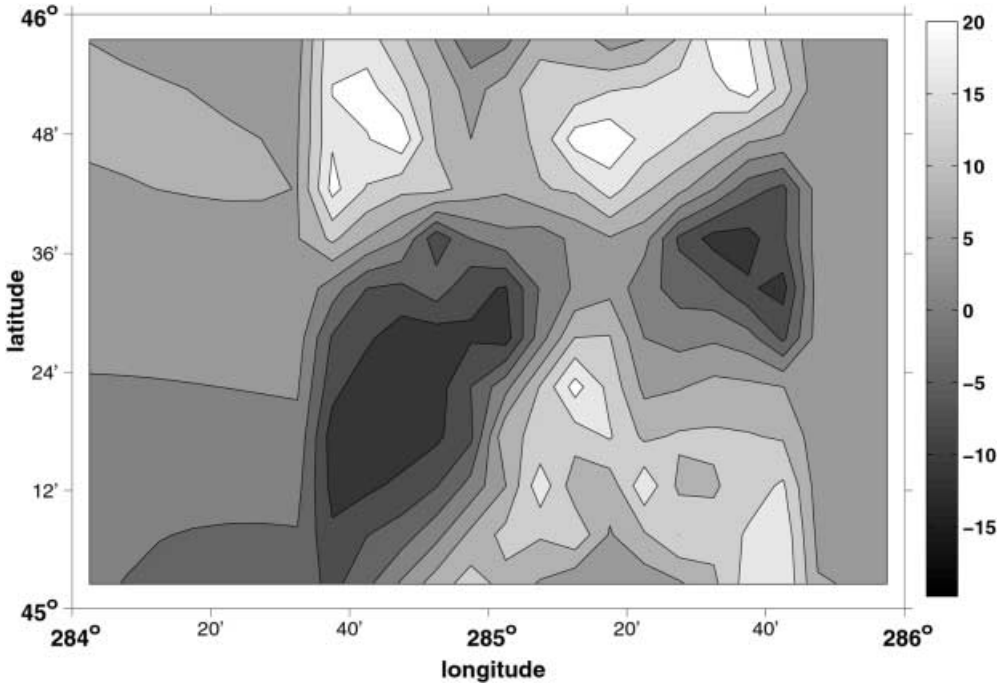

Fig. 10. Combined airborne and global gravity field for $181 \leq n \leq 360$–2000 (mGal)

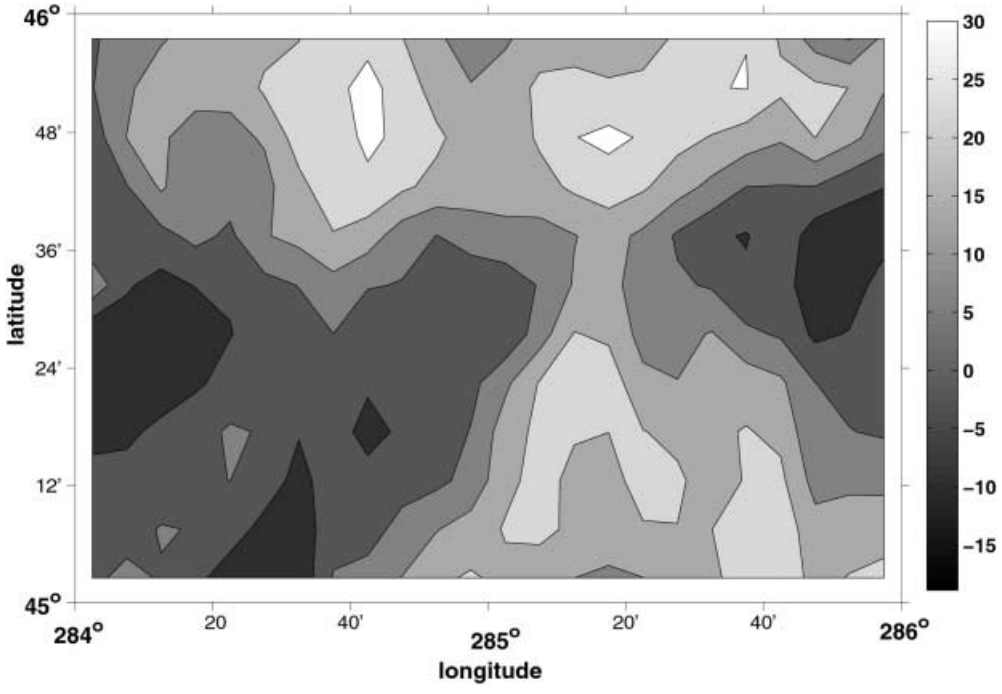

Fig. 11. Combined airborne and ground gravity field for $181 \leq n \leq 2000$ (mGal)

derived by applying the Bruns formula to the results of the Stokes integration.

The residual errors of the first geoid model, based on the combination of airborne and global gravity data, are shown in Fig. 13. The residual errors of the second geoid model, based on the combination of airborne and ground gravity data, are shown in Fig. 14. In both cases the values of the residual errors were obtained by referring these two solutions to the reference geoid. Statistical values of the residual errors are shown in Table 5. The solution based on the combination of the band-limited airborne and global gravity data has a slightly worse fit than the solution based on the band-limited airborne and ground data. Both solutions provided a very good agreement to the reference solution, which confirms that the airborne data can successfully be used for accurate geoid determination. The values in Table 5 correspond to a relative accuracy of approximately 20% (5 vs 25 cm). These values represent, however, the fit of two solutions based on different noisy gravity data sets. From this perspective, and from the perspective of accuracies obtained for the synthetic data in Table 4, these results are

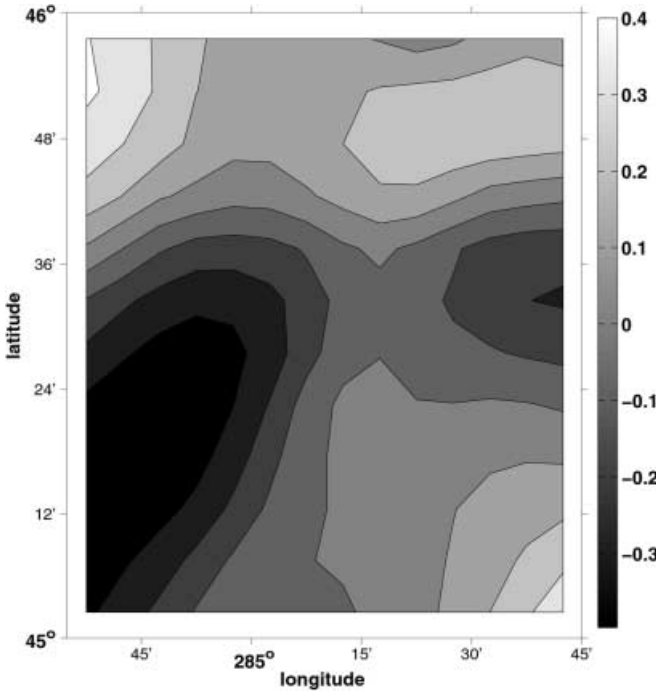

Fig. 12. Reference band-limited geoid computed from ground gravity (m)

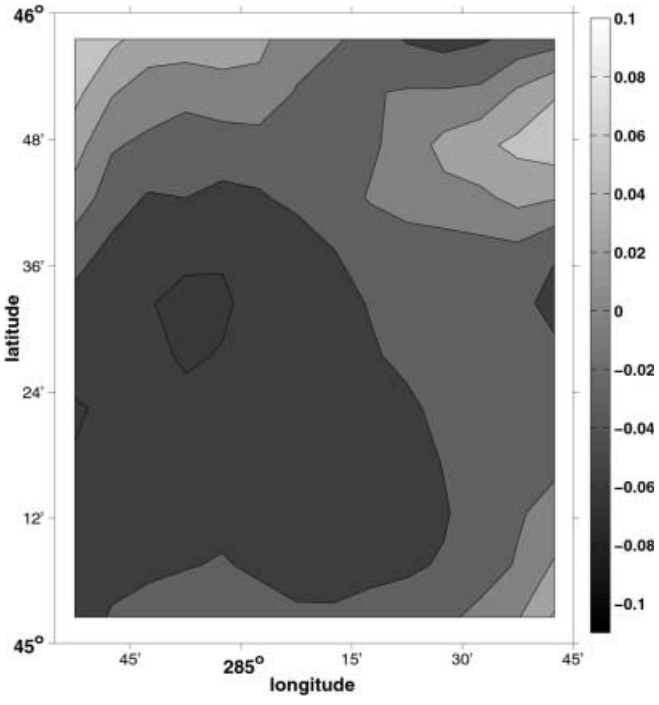

Fig. 13. Residual errors of the band-limited geoid based on airborne and global gravity (m)

very promising. It should be emphasized that no additional corrections, such as a bias and/or linear trend removal, were applied, which is common practice in many geoid computations. The accuracy of the total geoid would further be affected by the accuracy of the degree 2–180 geoid that can be computed from the GGM with a relative accuracy of approximately 1% in the test area. For the degree 2–180 geoid, this error would reach about 35 cm. It is expected that this accuracy will be significantly improved by the dedicated satellite missions, at least for the spherical harmonic degrees $n \leq 300$.

5 Conclusions

The scheme for geoid determination from airborne data (see Fig. 1) consists of the following operations:

- low-pass filtering of observed gravity disturbances to remove high-frequency observation noise;
- removal of the reference gravity from the low-passed gravity disturbances using a GGM;
- reduction of band-limited gravity disturbances using the corresponding direct effect on gravity;
- prediction of reduced band-limited gravity disturbances on a regular geographical grid;
- transformation of reduced band-limited gravity disturbances into the disturbing potential;
- reduction of the band-limited disturbing potential using the corresponding indirect effect;
- transformation of the disturbing gravity potential into the band-limited geoid;
- addition of the reference geoid to the band-limited geoid.

This computation scheme for geoid determination was tested using both band-limited synthetic and actually observed (using an inertially referenced airborne gravimeter) airborne gravity data over the Alexandria test range near Ottawa, Canada. Results obtained for the synthetic airborne gravity data provided information on the maximum accuracy of the geoid model achievable with the accuracy and typical geographical coverage of currently available airborne gravity data. This test indicated that the numerical and model accuracy of the approach is at the centimetre level, neglecting all possible errors originating from an incomplete and/or inaccurate gravity/co-geoid reduction. The actual accuracy of the current geoid models, especially over mountainous areas, however, would be at least one order of magnitude worse.

Two band-limited geoid models were computed combining the actual airborne gravity data with either global or ground gravity data. Both geoid models were compared with the reference geoid computed only from the ground gravity data. The accuracy of this reference model, neglecting any low-frequency bias, is expected to be at the centimetre level. The first geoid model, based on combination of the band-limited airborne and global gravity data, had a standard deviation of 5.5 cm. The second geoid model, based on combination of the band-limited airborne and ground gravity data, had a standard deviation of 4.7 cm. Values of the standard deviations were computed from the residual errors obtained by comparison of both models to the reference geoid; see Figs. 13, 14 and Table 5. Both accuracies refer only to the band-limited part of the geoid spectrum, neglecting the low-frequency bias in the solutions. This is justifiable

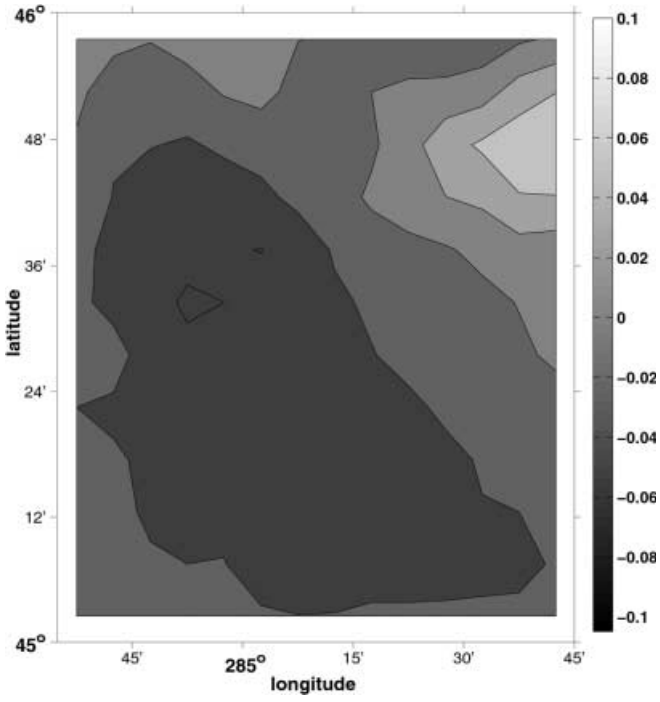

Fig. 14. Residual errors of the band-limited geoid based on airborne and ground gravity (m)

Table 5. Comparison of computed geoid models versus the reference geoid (m)

Solution	Minimum	Maximum	Mean	Sigma	RMS
Reference	−0.391	0.404	0.068	0.246	0.261
Reference–airborne and GGM	−0.110	0.145	−0.031	0.055	0.063
Reference–airborne and ground	−0.105	0.142	−0.035	0.047	0.059

with respect to the extent of the airborne gravity data used for geoid determination.

The obtained results proved the applicability of airborne gravity data for determination of the medium- to high-frequency components of the gravimetric geoid. Both applications can successfully be used for geoid determination with relatively high accuracy, assuming that the low-frequency geoid can be accurately computed from the GGM. The knowledge of the reference gravity field should improve significantly in the near future due to the forthcoming satellite missions dedicated to the mapping of the global gravity field. A combination of the satellite and airborne gravity data could then be used for an effective geoid mapping over all wavelengths.

Acknowledgements. Financial support for this research through the Canadian GEOIDE Network of Centres of Excellence within the project 'Airborne Gravity for Exploration and Mapping', and to Prof. B. Heck by the German Research Foundation (DFG), is gratefully acknowledged. The authors wish to thank Mr. Marc Véronneau of Natural Resources Canada for providing all the necessary ground gravity and elevation data.

References

Argyle M, Ferguson S, Sander L, Sander S (2000) AIRGrav results: a comparison of airborne gravity data with GSC test site data. Lead Edge October: 1134–1138

Bruton AM (2000) Improving the accuracy and resolution of SINS/DGPS airborne gravimetry. Ph.D. Thesis, UCGE rep. 20145, The University of Calgary

Forsberg R, Hehl K, Bastos B, Giskehaug A, Meyer U (1996) Development of an airborne geoid mapping system for coastal oceanography (AGMASCO). In: Segawa J, Fujimoto F, Okubo S (eds.) Gravity, Geoid and Marine Geodesy, IAG Symposia 117, Springer, Berlin, Heidelberg, New York: 163–170

Heck B (1993) A revision of Helmert's second method of condensation in the geoid and quasigeoid determination. In: Montag H, Reigber C (eds.) Geodesy and Physics of the Earth, IAG Symposia 112, Springer, Berlin, Heidelberg, New York: 246–251

Heiskanen WA, Moritz H (1967) Physical geodesy. WH Freeman, San Francisco

Hobson EW (1931) The theory of spherical and ellipsoidal harmonics. Chelsea, New York

Holota P (2000) Direct methods in physical geodesy. In: Schwarz KP (ed.) Geodesy beyond 2000. The challenges of the first decade. IAG Symposia 121, Springer, Berlin, Heidelberg, New York: 163–170

Kearsley AHW, Forsberg R, Olesen A, Bastos L, Hehl K, Meyer U, Gidskehaug A (1998) Airborne gravimetry used in precise geoid computations by ring integration. J Geod 72: 600–605

Lemoine FG, Kenyon SC, Factor JK, Trimmer RG, Pavlis NK, Chinn DS, Cox CM, Klosko SM, Luthcke SB, Torrence MH, Wang YM, Williamson RG, Pavlis EC, Rapp RH, Olson TR (1998) The development of the joint NASA GSFC and NIMA geopotential model EGM96. NASA/TP-1998-206861, NASA/GSFC, Greenbelt, Maryland

Moritz H (1980) Advanced physical geodesy. Wichmann, Karlsruhe

Novák P, Heck B (2002) Downward continuation and geoid determination based on band-limited airborne gravity data. J Geod 76: 269–278

Novák P, Kern M, Schwarz KP, Heck B (2001) On the determination of the gravimetric geoid from airborne gravity. UCGE tech rep 30013, The University of Calgary

Paul M (1973) A method of evaluation the truncation error coefficients for geoidal heights. Bull Géod 110:413-425

Véronneau M (1995) Scientific model of the Canadian gravimetric geoid GSD95. Geodetic Survey Division, Natural Resources Canada, Ottawa (Canadian geoid package GPS·H distributed on CD)

Wenzel HG (1998) Ultra-high degree geopotential models GPM98 A, B, and C to degree 1800. Presented at Joint Meeting Int Gravity Commission and Int Geoid Commission, 7–12 September, Trieste (www://www.gik.uni-karlsruhe.de/~wenzel/papers.htm)

Wenzel HG (1999) Ultra-high degree spherical harmonic models of the Earth's topography, rock equivalent topography and topographic isostatic potential. Presented at EGS General Assembly, 10–16 May, Den Haag (www://www.gik.uni-karlsruhe.de/~wenzel/geopmods.htm)